Dynamic structure factor in warm dense beryllium

2012 New J. Phys. 14 055020

(http://iopscience.iop.org/1367-2630/14/5/055020)

New Journal of Physics
The open-access journal for physics

Dynamic structure factor in warm dense beryllium

K-U Plagemann[1,7], P Sperling[1], R Thiele[2], M P Desjarlais[3], C Fortmann[4,5], T Döppner[5], H J Lee[6], S H Glenzer[5] and R Redmer[1]

[1] Institut für Physik, Universität Rostock, 18051 Rostock, Germany
[2] Center for Free-Electron Laser Sciences, DESY, Notkestraße 85, 22607 Hamburg, Germany
[3] Pulsed Power Sciences Center, Sandia National Laborartories, Albuquerque, NM 87158-1186, USA
[4] Department of Physics and Astronomy, University of California-Los Angeles, Los Angeles, CA 90095, USA
[5] Lawrence Livermore National Laboratory, PO Box 808, Livermore, CA 94551, USA
[6] SLAC National Accelerator Laboratory, 2575 Sand Hill Road, Menlo Park, CA 94025, USA
E-mail: kai-uwe.plagemann@uni-rostock.de

New Journal of Physics **14** (2012) 055020 (13pp)
Received 31 January 2012
Published 21 May 2012
Online at http://www.njp.org/
doi:10.1088/1367-2630/14/5/055020

Abstract. We calculate the dynamic structure factor (DSF) in warm dense beryllium by means of *ab initio* molecular dynamics simulations. The dynamic conductivity is derived from the Kubo–Greenwood formula, and a Drude-like behaviour is observed. The corresponding dielectric function is used to determine the DSF. Since the *ab initio* approach is so far only applicable for wavenumbers $k = 0$, the k-dependence of the dielectric function is modelled via the Mermin ansatz. We present the results for the dielectric function and DSF of warm dense beryllium and compare these with perturbative treatments such as the Born–Mermin approximation. We found considerable differences between the results of these approaches; this underlines the need for a first-principles determination of the DSF of warm dense matter.

[7] Author to whom any correspondence should be addressed.

Contents

1. Introduction

A key issue of plasma diagnostics is the determination of plasma parameters such as, e.g., the free-electron density and temperature. This task is hampered in dense plasmas since fundamental quantities such as cross-sections, ionization state and conductivities are affected by strong correlations and quantum effects so that the known simple approximations are no longer applicable. Therefore, consistent many-particle approaches have to be developed and checked with benchmarking experiments. A versatile and reliable tool for this purpose is x-ray Thomson scattering (XRTS) [1, 2], which gains the plasma parameters directly from the dynamic structure factor (DSF) [3]. X-rays penetrate dense matter, and intense x-ray sources are now available to perform scattering experiments. For instance, intense x-ray pulses are produced either by energetic optical lasers or by free-electron lasers in the soft or hard x-ray regimes.

X-rays emitted from laser-produced plasmas [4, 5] can probe the region from warm dense matter (WDM) [6, 7] with temperatures of several eV and densities close to solid density [8–10] up to compressed matter well above solid density and at electron temperatures of 0.1 eV and several tens of eV [11–14][AQ ID=Q1]. The outstanding applications of XRTS are, e.g., in-flight measurements of laser-driven implosion dynamics of inertial confinement fusion capsules [15] and of radiative heating and cooling dynamics of matter [16], both on ns time scales. Plasmas in the near-solid density regime have also been probed by combining optical lasers (pump) and soft x-rays (probe) [17].

The plasma parameters electron temperature T_e, free-electron density n_e and the mean ionization state Z can be derived by analyzing the XRTS signal. The electron temperature can be inferred from the universal detailed balance relation, whereas the electron density follows from the plasmon dispersion in the collective scattering mode [8, 18, 19].

XRTS experiments have been performed on beryllium for different conditions [8, 10, 12, 20]. It is a potential ablator material in inertial confinement fusion capsules [21] and also relevant for astrophysics considering the neutrino capture reactions in the Sun and the problem of neutrino oscillations [22]. In this paper, we determine the DSF for uncompressed beryllium (u-Be [10]: $T_e = 12\,\mathrm{eV}$, $\rho = 1.85\,\mathrm{g\,cm^{-3}}$) and threefold compressed beryllium (c-Be [12]: $T_e = 13\,\mathrm{eV}$, $\rho = 5.5\,\mathrm{g\,cm^{-3}}$), thereby studying the effect of strong correlations characterized by electron coupling parameters

$$\Gamma_e = \frac{e^2}{4\pi\epsilon_0 k_B T_e}\left(\frac{4\pi n_e}{3}\right)^{1/3} \geqslant 1, \tag{1}$$

and the effect of degeneracy as relevant for electron degeneracy parameters

$$\Theta_e = \frac{2m_e k_B T_e}{\hbar^2}\left(3\pi^2 n_e\right)^{-2/3} \leqslant 1. \tag{2}$$

Theoretical efforts usually start with the implementation of the DSF as the basic input for the Thomson scattering cross-section on the level of the random phase approximation (RPA) as was shown in [9]. The influence of electron–ion collisions on the DSF within the first Born approximation can be studied in addition based on the dynamic collision frequency $\nu(\omega)$ [23]. A systematic improvement of the Born approximation including dynamic screening, strong collisions and electron–electron collsions has been accomplished as well [24, 25]. This treatment can be extended to finite wavenumbers k by using the Mermin ansatz for the dielectric function [26–28] in order to calculate the DSF at arbitrary k.

In this paper, we determine the DSF via *ab initio* simulations. This method treats quantum and correlation effects beyond the RPA and perturbative treatments and is thus suited for treating WDM. It has been demonstrated that *ab initio* results for the equation of state [29–31] and the electrical and thermal conductivity of various materials [32, 33] are in very good agreement with shock-wave experiments. Here we use finite-temperature density functional theory molecular dynamics (FT-DFT-MD) simulations to calculate the dynamic conductivity $\sigma(\omega)$ and thus the dynamic collision frequency $\nu(\omega)$. We found that the corresponding DSF for $k = 0$ derived from the fluctuation–dissipation theorem agrees well with that obtained from the Mermin dielectric function [26]. Assuming that the k-dependence of the dielectric function follows the Mermin ansatz, we calculate the DSF for arbitrary wavenumbers k. This allows us to calculate the complete k and ω resolved structure factors using the FT-DFT-MD method, whereas previous studies were limited to static or dynamic properties alone. Finally, we compare our results with the Born–Mermin approximation (BMA).

The outline of the paper is as follows. We present the theory for the DSF in section 2 and summarize the details of *ab initio* simulations in section 3. We give there the results on the ion–ion pair distribution function, the respective structure factor and the dynamic conductivity of warm dense beryllium. The results on the dielectric function and DSF are presented in section 4. The conclusions drawn are presented in section 5.

2. Theory of the dynamic structure factor (DSF)

We start with the scattered power per solid angle $\mathrm{d}\Omega = \sin\theta\,\mathrm{d}\theta\,\mathrm{d}\varphi$ and per unit frequency interval $\mathrm{d}\omega$, which is experimentally accessible and given by the following expression [3]:

$$\frac{\mathrm{d}^2 P_{sc}}{\mathrm{d}\Omega \mathrm{d}\omega} = \frac{\sigma_T}{A_{rad}}\frac{k_f}{k_i}\int_{-\infty}^{\infty}\frac{\mathrm{d}\omega'}{2\pi} G_{\Delta\omega}(\omega-\omega')\int \mathrm{d}^3\mathbf{r}\, l(\mathbf{r}) S_{ee}(\mathbf{k},\omega') n_e(\mathbf{r}). \tag{3}$$

Here, $\sigma_T = 6.65\times10^{-24}\,\mathrm{cm}^2$ is the Thomson scattering cross-section, k_i and k_f are the initial and final photon wavenumbers and the energy and momentum transfer are given by $\Delta E = \hbar\omega = \hbar\omega_f - \hbar\omega_i$ and $\hbar\mathbf{k} = \hbar\mathbf{k}_f - \hbar\mathbf{k}_i$. The central quantity for the determination of the scattering signal is the DSF $S_{ee}(\mathbf{k},\omega)$, which can be calculated for given profiles of electron density $n_e(\mathbf{r})$, electron temperature $T_e(\mathbf{r})$, ion density $n_i(\mathbf{r})$ and ion temperature $T_i(\mathbf{r})$, i.e. for the general case of an inhomogeneous target. Therefore, we consider in this paper only the DSF for simplicity. The momentum is related to the scattering angle θ in the limit $\hbar\omega \ll \hbar\omega_0$ according to $k = 4\pi\sin(\theta/2)/\lambda_0$, with λ_0 being the probe wavelength. $l(\mathbf{r})$ is the $\mathbf{r}$-dependent power density

of the probe beam taking into account absorption in the target, and A_{rad} is the irradiated surface of the target. The DSF has to be convoluted with the instrumental function $G_{\Delta\omega}(\omega)$ that models the spectrometer's finite spectral resolution as well as the probe's spectral bandwidth. Usually, a normalized Gaussian distribution is employed with the full-width at half-maximum $\Delta\omega$.

The DSF can be written in terms of free–free, bound–free and bound–bound correlations as proposed by Chihara [34, 35]. In this paper, we consider the contribution of free electrons $S^0_{\mathrm{ee}}(k, \omega)$, which is connected to the longitudinal dielectric function $\epsilon(k, \omega)$ via the fluctuation-dissipation theorem (FDT),

$$S^0_{\mathrm{ee}}(k, \omega) = -\frac{\epsilon_0 \hbar k^2}{\pi e^2 n_{\mathrm{e}}} \frac{\mathrm{Im}\,\epsilon^{-1}(\mathrm{k}, \omega)}{1 - \exp\left(-\frac{\hbar\omega}{k_{\mathrm{B}} T_{\mathrm{e}}}\right)}. \tag{4}$$

Bound–bound correlations have to be studied to determine the elastic scattering signal, which is known as ion feature. The corresponding static structure factors have been calculated for beryllium in [36]. Bound–free transitions are important for photon energies that are much larger than the plasma frequency in beryllium, see section 3. Both contributions will be studied in future work in order to make a comparison with full experimental scattering spectra.

Considering free electrons without interactions the dielectric function is given by the RPA for the one-component plasma. Including interactions between the particles in the plasma via the dynamic electron–ion collision frequency $\nu(\omega)$ [28], the more general approach of Mermin [26] can be applied to the dielectric function, which then reads

$$\epsilon^{\mathrm{M}}(k, \omega) - 1 = \frac{\left(1 + \mathrm{i}\frac{\nu(\omega)}{\omega}\right)\left[\epsilon^{\mathrm{RPA}}(k, \omega + \mathrm{i}\nu(\omega)) - 1\right]}{1 + \mathrm{i}\frac{\nu(\omega)}{\omega}\frac{\epsilon^{\mathrm{RPA}}(k, \omega + \mathrm{i}\nu(\omega)) - 1}{\epsilon^{\mathrm{RPA}}(k, 0) - 1}}. \tag{5}$$

Calculating the electron–ion collision frequency in the Born approximation defines the BMA; see [18, 19, 23, 37]. A further improvement of the BMA is achieved by including correlations between the electrons via local field corrections (LFC) $G(k, \omega)$ [38]. The dielectric function in this BMA–LFC approach reads

$$\epsilon(k, \omega) = 1 - \frac{1 - \epsilon^{\mathrm{RPA}}(k, \omega)}{1 + G(k, \omega)[1 - \epsilon^{\mathrm{RPA}}(k, \omega)]}. \tag{6}$$

For $G(k, \omega)$ we use the dynamic LFC as given by Ichimaru and Utsumi [39].

A further analysis of the DSF and the Thomson scattering process is possible via the scattering parameter $\alpha = \kappa/k$, which relates the inverse screening length κ to the wavenumber k. For $\alpha < 1$ the scattering is non-collective and we can investigate short-range correlations, while long-range correlations are relevant for collective scattering ($\alpha > 1$). In the case of long-range correlations the DSF $S^0_{\mathrm{ee}}(k, \omega)$ shows two particularly pronounced side maxima which are located symmetrically relative to the central ion feature. These peaks are directly related to the free-electron density via the plasmon frequency; see also [10, 18, 19].

3. Finite-temperature density functional theory molecular dynamics simulations

Another possibility to calculate the dielectric function is to perform *ab initio* simulations. The FT-DFT-MD framework combines classical MD simulations for the ions with a quantum treatment of the electrons based on FT-DFT [26, 40, 41]. We use its implementation in the Vienna *ab initio* simulation package VASP 4.6.28 [42–44] and the provided projector augmented wave [45, 46] all-electron pseudopotential for the interaction between the nuclei

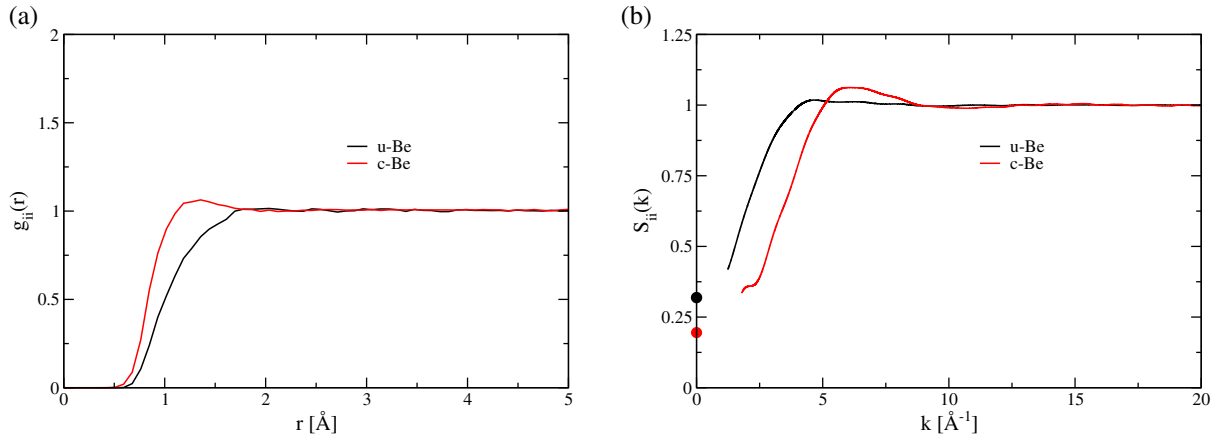

Figure 1. Ion–ion pair distribution function $g_{ii}(r)$ (a) and static structure factor $S_{ii}(k)$ (b) for u-Be (black line: $T = 12\,\mathrm{eV}$ and $\rho = 1.85\,\mathrm{g\,cm^{-3}}$) and c-Be (red line: $T = 13\,\mathrm{eV}$ and $\rho = 5.5\,\mathrm{g\,cm^{-3}}$). The values at $k = 0$ are calculated via the isothermal compressibility.

and the electrons within the DFT. The exchange and correlation term is approximated by the functional of Perdew, Burke and Ernzerhof [47] for all simulations. Convergence was checked with respect to the particle numbers which vary between 32 and 256 atoms, the **k**-point sets used for the evaluation of the Brillouin zone and the energy cutoff for the plane wave basis set. With these results the simulations were finally carried out with a particle number of 32 beryllium atoms with 4 electrons each, an energy cutoff of 1400 eV and a simulation time up to 20 ps. The ion temperature was controlled with a Nosé thermostat [48]. The evaluation of the Brillouin zone was made at the Baldereschi mean value point [49].

In order to demonstrate the power of the FT-DFT-MD simulations, we first determined the equation of state and the ion–ion pair distribution function $g_{\mathrm{ii}}(r)$ of warm dense beryllium for the parameters of the XRTS experiments, i.e. for u-Be [10] and c-Be [12]. The respective static ion–ion structure factors $S_{\mathrm{ii}}(k)$ were determined via the Fourier transform of the ion–ion pair distribution functions as obtained from the FT-DFT-MD simulations,

$$S_{\mathrm{ii}}(k) = 1 + n_{\mathrm{i}} \int g_{\mathrm{ii}}(r)\, \mathrm{e}^{\mathrm{i}\vec{k}\vec{r}}\, \mathrm{d}\vec{r}. \tag{7}$$

The ion–ion pair distribution function and the ion–ion structure factor are shown in figure 1 for u-Be and c-Be. An increase in density results in a stronger peak of the ion–ion pair distribution function, which is also shifted towards smaller distances due to stronger correlation. The peak of the corresponding ion–ion structure factor is shifted towards higher k values with increasing density and its height is more pronounced. Due to the finite size of the simulation box, the structure factor cannot be determined for small wavenumbers k. However, its starting point at $k = 0$ is given by the isothermal compressibility which is calculated from the corresponding equation of state data that were derived from the FT-DFT-MD simulations as well. The results shown in figure 1 are in agreement with earlier results [36] and can be used to determine the ion feature of the XRTS spectrum, see [34, 35, 50–52]. We focus here on the electronic part of the scattering spectrum.

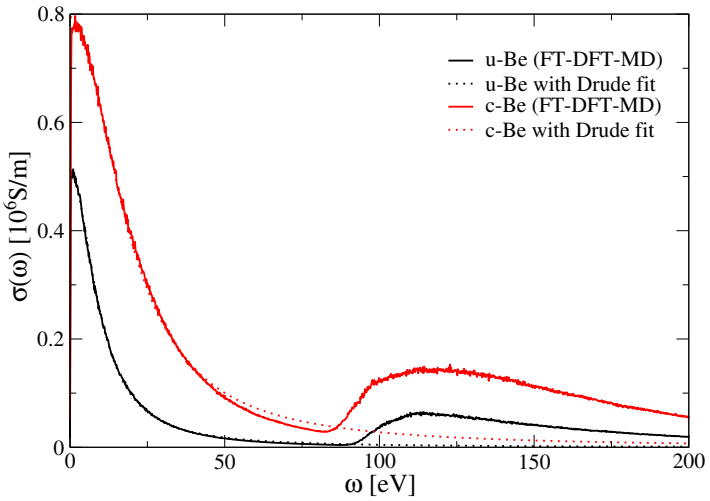

Figure 2. Dynamic conductivity for u-Be (black line: $T = 12\,\mathrm{eV}$ and $\rho = 1.85\,\mathrm{g\,cm^{-3}}$) and c-Be (red line: $T = 13\,\mathrm{eV}$ and $\rho = 5.5\,\mathrm{g\,cm^{-3}}$). Above a photon energy of 80 eV (c-Be) and 90 eV (u-Be) the K-shell electrons are excited. For lower energies, an almost perfect Drude-like behaviour (dotted lines) is observed.

Furthermore, we extract the electrical conductivity from the FT-DFT-MD simulations, which determines the dielectric function. The real part of the dynamic conductivity $\sigma(\omega)$ is calculated via the Kubo–Greenwood formula [53, 54], see [31–33]. Evaluations are perfomed for ten ion configurations (snapshots) from an equilibrated MD simulation using the Monkhorst–Pack **k**-point meshes [55] of $3 \times 3 \times 3$ and a cut-off energy of 1400 eV; the average is performed subsequently. The imaginary part of $\sigma(\omega)$ follows from a Kramers–Kronig relation, and the total dielectric function is given by

$$\mathrm{Re}\,\epsilon(\omega) = 1 - \frac{1}{\epsilon_0 \omega}\mathrm{Im}\,\sigma(\omega), \tag{8}$$

$$\mathrm{Im}\,\epsilon(\omega) = \frac{1}{\epsilon_0 \omega}\mathrm{Re}\,\sigma(\omega). \tag{9}$$

The results for the dielectric function as obtained from the FT-DFT-MD simulations are then used to determine the DSF via the FDT (equation (4)).

The dynamic collision frequency $\nu(\omega)$ is related to the dynamic conductivity $\sigma(\omega)$ in the long-wavelength limit via a generalized Drude expression [24, 27],

$$\sigma(\omega) = \frac{\epsilon_0 \omega_{\mathrm{pl}}^2}{-\mathrm{i}\omega + \nu(\omega)}, \tag{10}$$

with the electron plasma frequency $\omega_{\mathrm{pl}}^2 = n_e e^2/(\epsilon_0 m_e)$. This allows us to relate the electrical conductivity via the real part of the Drude formula (equation (10)),

$$\mathrm{Re}\,\sigma^{\mathrm{D}} = \frac{\sigma_0}{1 + \omega^2 \tau^2}, \tag{11}$$

with σ_0 being the static conductivity at $\omega = 0$ and $\tau = 1/\nu$ being the relaxation time.

Our numerical results on the dynamic conductivity are shown in figure 2. Both curves show an almost perfect Drude-like behaviour for $\omega \leqslant 80\,\mathrm{eV}$ (c-Be) and $\omega \leqslant 90\,\mathrm{eV}$ (u-Be),

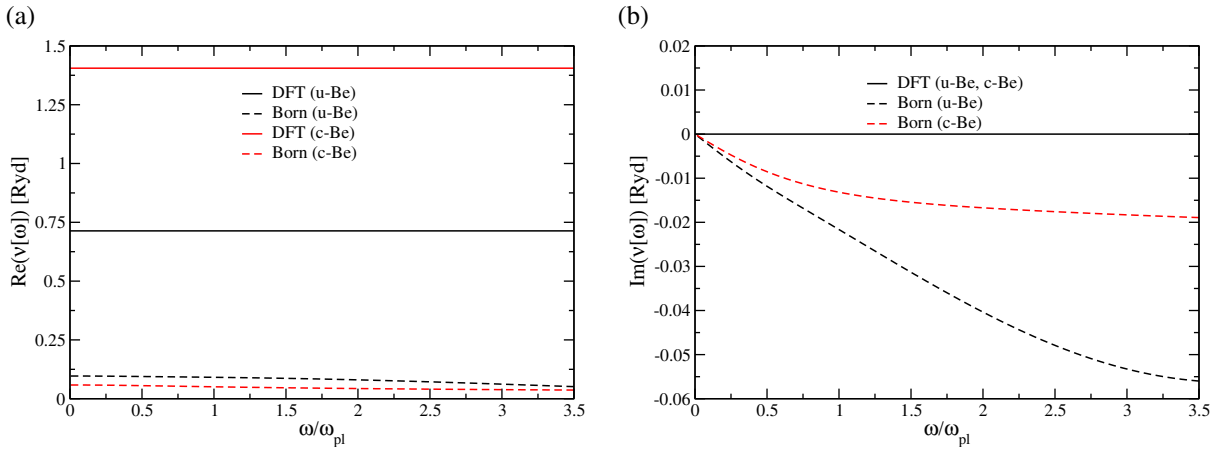

Figure 3. Dynamic collision frequency for u-Be ($T_e = 12\,\mathrm{eV}$ and $n_e = 2.61 \times 10^{23}\,\mathrm{cm}^{-3}$) and c-Be ($T_e = 13\,\mathrm{eV}$ and $n_e = 8.13 \times 10^{23}\,\mathrm{cm}^{-3}$): real parts (a), imaginary parts (b). We compare the DFT results derived from the dynamic conductivity (figure 2) within the Drude model, equation (10), with the first Born approximation used in the Mermin dielectric function, equation (5).

respectively. For larger energies, interband transitions from the K-shell become relevant, which are not considered in what follows because their threshold energy is much larger than the plasma frequency. A static collision frequency is sufficient for describing this Drude-like behaviour of the dynamic conductivity according to equation (11). The corresponding fit for u-Be yields a free-electron density $n_e = 2.61 \times 10^{23}\,\mathrm{cm}^{-3}$, an ionization degree $Z = 2.105$, an electron plasma frequency $\omega_{\mathrm{pl,e}} = 18.97\,\mathrm{eV}$ and a collision frequency $\nu = 9.71\,\mathrm{eV}$. This corresponds to a coupling parameter $\Gamma_e = 1.24$ and a degeneracy parameter $\Theta_e = 0.8$. For c-Be we extract the values $n_e = 8.13 \times 10^{23}\,\mathrm{cm}^{-3}$, $Z = 2.21$, $\omega_{\mathrm{pl,e}} = 33.48\,\mathrm{eV}$ and $\nu = 19.12\,\mathrm{eV}$, which yields the plasma parameters $\Gamma_e = 1.68$ and $\Theta_e = 0.4$. The increase in the ionization degree due to compression ($Z = 2.105 \rightarrow Z = 2.21$) is small because the energy gap to the K-shell electrons is still huge. In principle, the shift of the K-edge with density and temperature can be used as a diagnostic tool; see, e.g., [56].

This constant and real collision frequency contains the exchange and correlation effects in warm dense beryllium as treated within DFT. The stronger correlations in c-Be can be seen directly from the collision frequency, which is doubled compared with u-Be. Furthermore, we compare in figure 3 these collision frequencies for u-Be and c-Be with the Born approximation with respect to a statically screened potential which is used in the BMA. The DFT results for the real part are higher than the Born approximation by a factor of more than 7 (u-Be) and 23 (c-Be), while no imaginary parts occur. The impact of these substantially different results on the dielectric function and DSF will be discussed in the next section.

4. Results on the dielectric function and DSF

The dielectric function can be used to determine the DSF via the FDT, equation (4). Until now FT-DFT-MD simulations are possible only for $k = 0$, i.e. in the long-wavelength limit. To extend these calculations also to finite wavenumbers $k > 0$, i.e. to compare with XRTS

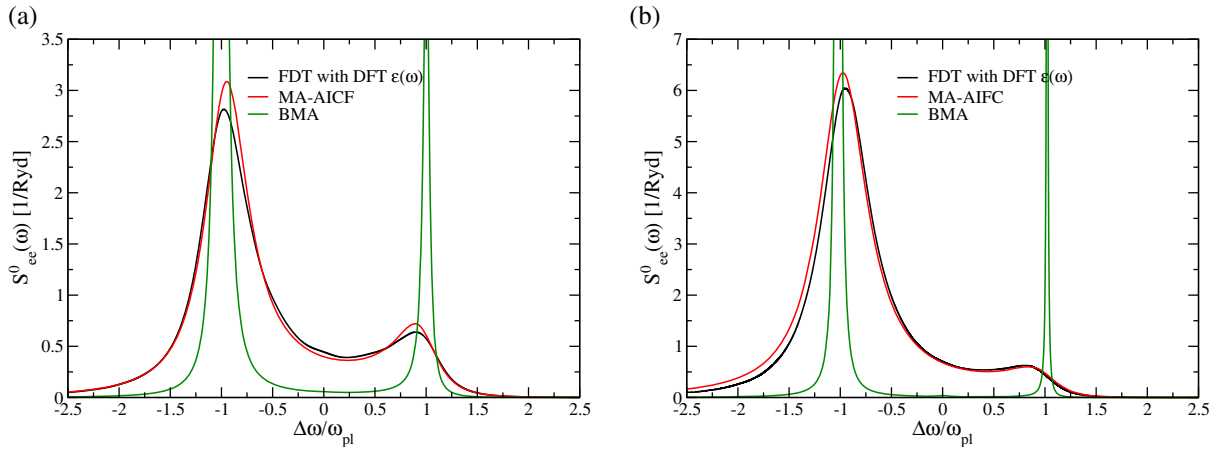

Figure 4. DSF derived from the FDT (4) for u-Be ((a) $T_e = 12\,\mathrm{eV}$ and $n_e = 2.61 \times 10^{23}\,\mathrm{cm}^{-3}$) and c-Be ((b) $T_e = 13\,\mathrm{eV}$ and $n_e = 8.13 \times 10^{23}\,\mathrm{cm}^{-3}$) in the long-wavelength limit $k \to 0$ using the dielectric function from the FT-DFT-MD simulations according to equations (8)–(9) (black), the MA-AICF (red) and the BMA (green).

experiments at given scattering angles, we apply again the Mermin ansatz, equation (5), and calculate the dielectric function with the collision frequency as derived from FT-DFT-MD simulations for $k = 0$. In the following, we call this method the Mermin approximation with *ab initio* collision frequencies (MA-AICF), in contrast to the perturbative treatment of collisions in the Born–Mermin approximation (BMA).

We check the performance of this method in the long-wavelength limit where the *ab initio* results on the dynamic conductivity shown in figure 2 yield the dielectric function directly via equations (8) and (9). Inserting this dielectric function into the FDT equation (4), the DSF is determined for $k = 0$ solely based on first principles. This result (black line) is compared in figure 4 with the BMA (green line) and the MA-AICF (red line) for $k \to 0$. Both approximations treat the k-dependence of the dielectric function via the Mermin dielectric function equation (5), while collisions are considered perturbatively (Born approximation: BMA) or *ab initio* (DFT: MA-AICF). For $k \to 0$ the MA-AICF curve agrees well with the first-principles result. The plasmon peaks obtained in the BMA are much sharper and located at slightly higher frequencies. In the following, we apply the MA-AICF also to finite wavenumbers k and compare with the BMA.

The real and imaginary parts of the dielectric function are shown in figures 5 and 6 for u-Be and c-Be, respectively, for the three scattering angles $\theta = 20^\circ$, 40° and 60° and a probe wavelength $\lambda_0 = 0.42\,\mathrm{nm}$ for u-Be and $\lambda_0 = 0.2\,\mathrm{nm}$ for c-Be. Overall, the imaginary part describes the damping of plasma excitations and zeros in the real part indicate collective motion of particles corresponding to plasma oscillations or plasmons. Both parts determine the DSF via the FDT, equation (4), according to

$$\mathrm{Im}\,\epsilon^{-1}(k,\omega) = -\frac{\mathrm{Im}\,\epsilon(k,\omega)}{[\mathrm{Re}\,\epsilon(k,\omega)]^2 + [\mathrm{Im}\,\epsilon(k,\omega)]^2}. \tag{12}$$

Plasmons result from conditions where the real part of the dielectric function has zeros or at least minima and, simultaneously, the imaginary part is small. Otherwise these modes will be

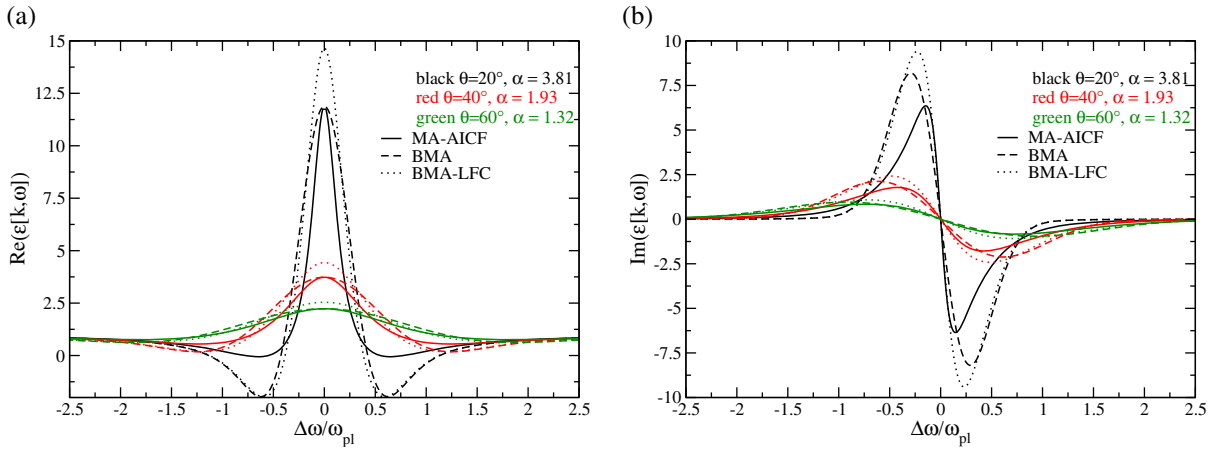

Figure 5. Real (a) and imaginary parts (b) of the dielectric function dependent on the photon energy in units of the plasma frequency for u-Be ($T_e = 12\,\mathrm{eV}$, $n_e = 2.61 \times 10^{23}\,\mathrm{cm}^{-3}$) for the three scattering angles $\theta = 20°$, $40°$ and $60°$: MA-AICF (solid), BMA with LFC (dotted) and without LFC (dashed).

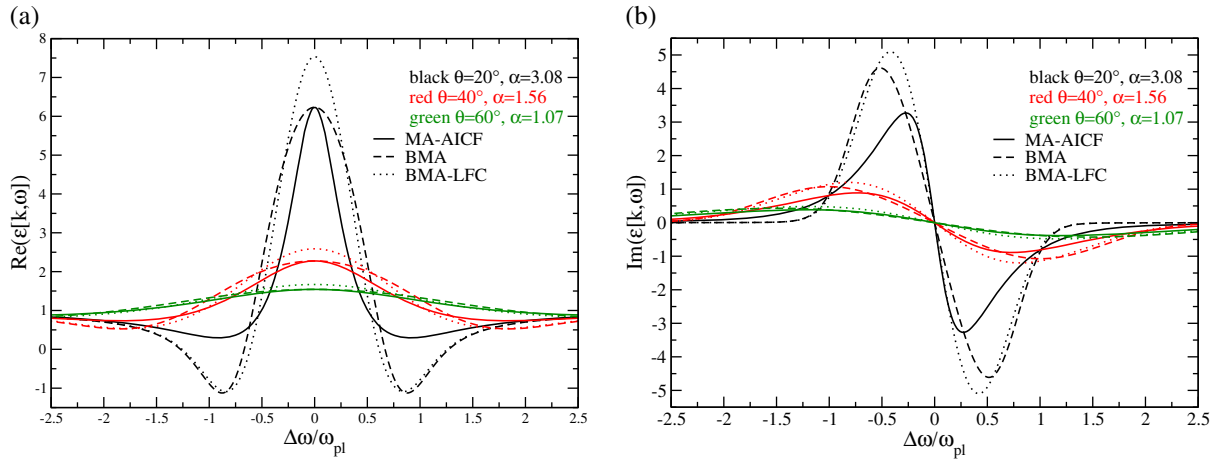

Figure 6. The same as figure 5 but for c-Be ($T_e = 13\,\mathrm{eV}$ and $n_e = 8.13 \times 10^{23}\,\mathrm{cm}^{-3}$).

damped strongly. Furthermore, plasmons can be observed via XRTS in the collective scattering regime, i.e. for $\alpha > 1$; for a more detailed discussion, see [10, 19, 57].

Figures 5 and 6 indicate that considerable deviations between the various approaches to the dielectric function occur only for small angles θ or wavenumbers k, i.e. for collective scattering $\alpha \gg 1$. Furthermore, zeros in the real part are observed only for u-Be at low scattering angles $\theta \leqslant 20°$. For all other cases the real part has only shallow minima which are shifted to higher frequencies. The consideration of LFC in the BMA [38] shifts the zeros/minima slightly to smaller frequencies as compared with the original BMA, while the imaginary parts have more pronounced peaks. The MA-AICF shifts the zeros/minima further to smaller frequencies, but the imaginary parts are smaller compared with both versions of the BMA. Furthermore, the peaks in both the real and imaginary parts have a smaller width than the BMA. This behaviour

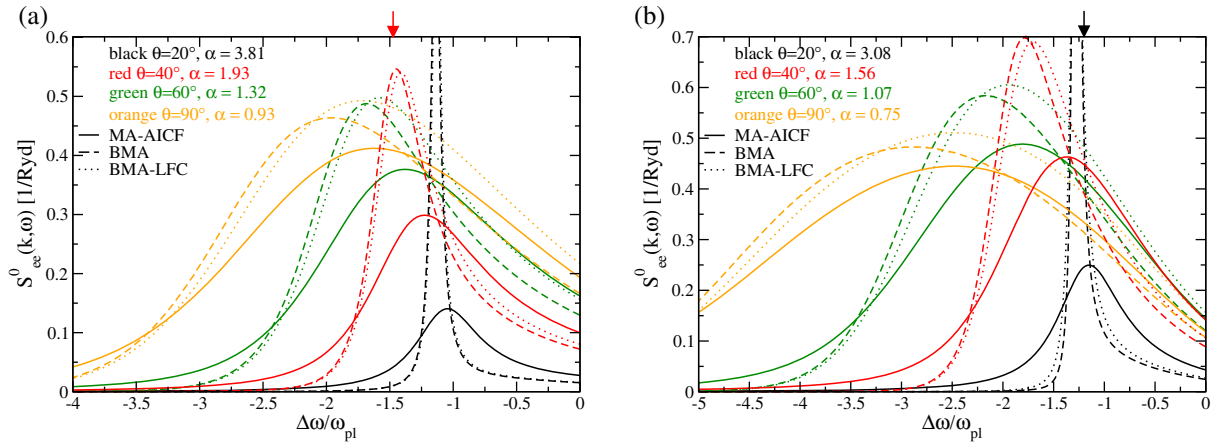

Figure 7. Dynamic structure factor for different angles, plotted for u-Be ((a) $T_e = 12\,\text{eV}$ and $n_e = 2.61 \times 10^{23}\,\text{cm}^{-3}$) and c-Be ((b) $T_e = 13\,\text{eV}$ and $n_e = 8.13 \times 10^{23}\,\text{cm}^{-3}$). We compare the MA-AICF (solid line) with the BMA with LFC (dotted line) and without LFC (dashed line). Arrows mark the location of the plasmon peaks as derived from XRTS experiments for u-Be at 40° [10] and for c-Be at 25° [12].

can be traced back to the much higher collision frequency in the MA-AICF, cf figure 3, and hence represents a correlation effect. These trends were already obtained by replacing the RPA dielectric function with the BMA when calculating the DSF [19].

The corresponding DSF is displayed in figure 7 for different scattering angles $\theta = 20°$, 40°, 60° and 90° and a probe wavelength $\lambda_0 = 0.42\,\text{nm}$ for u-Be and $\lambda_0 = 0.2\,\text{nm}$ for c-Be. For a better illustration, we show only the red-shifted left peak of the DSF. We observe a pronounced broadening of the plasmon peak for all angles in the MA-AICF, whereas the BMA with and without LFC shows such a behaviour only for larger angles $\theta > 20°$. The position of the plasmon peak in the MA-AICF is shifted towards lower frequencies relative to the BMA. For large scattering angles, both the MA-AICF and the BMA-LFC yield almost the same location for the plasmon resonance.

First XRTS experiments have probed the collective scattering regime in warm dense beryllium: at $\theta = 40°$ for u-Be [10] and at $\theta = 25°$ for c-Be [12]. The location of the measured plasmon resonance is marked by arrows in figure 7. The MA-AICF result for 20° yields very good agreement with the experimental point for c-Be. For u-Be the plasmon shift of the MA-AICF is smaller than the experimental point and the BMA. This indicates that the plasmon dispersion relation as predicted by the Mermin dielectric function (which relies on the RPA dielectric function for collisionless plasmas, see equation (5)) is modified for larger scattering angles θ or wavenumbers k.

The different behaviour of the DSF can be analyzed further by checking sum rules for the dielectric function used here,

$$\langle \omega^l \rangle_\pm = \int_{-\infty}^{\infty} \frac{\mathrm{d}\omega}{\pi} \omega^l \,\mathrm{Im}\,\epsilon^{\pm 1}(k,\omega). \tag{13}$$

The f-sum rule $\langle \omega^1 \rangle_- = -\omega_{\text{pl}}^2$ and the conductivity sum rule $\langle \omega^1 \rangle_+ = \omega_{\text{pl}}^2$ are always fulfilled. The third-moment sum rule via $l = 3$ tests the high-frequency behaviour of the dielectric

function. It is known that this sum rule is violated within a simple Drude approach, i.e. assuming a constant collision frequency ν [24]. However, as we have shown by our FT-DFT-MD simulations, the dynamic conductivity can be fitted very well by a constant collision frequency for $\omega < 50\,\mathrm{eV}$ within the Drude model, cf figures 2 and 3. For an improved treatment of the high-frequency behaviour of the dielectric function, we have to consider bound-free transitions beyond the Drude approximation as can be seen in figure 2. These contributions are usually described by an extra term in the Chihara formula; see [34, 35].

5. Summary

We have calculated the dielectric function and the DSF for uncompressed and threefold compressed beryllium based on FT-DFT-MD simulations. We found almost perfect Drude-like behaviour for the dynamic electrical conductivity. These *ab initio* results on the respective collision frequency are then used to determine the dielectric function for arbitrary wavenumbers k within the Mermin ansatz (5). Finally, we calculate the DSF for various scattering angles and compare our results with a perturbative treatment of collisions (BMA) [18] and with a generalization that considers also local-field corrections (BMA-LFC) [38]. Considerable differences for the location of the plasmon resonance and its width are observed. These predictions can be checked by first XRTS experiments that have already probed the collective scattering regime in warm dense beryllium. We found a very good agreement with the point for low-angle XRTS at 25° for c-Be [12]. The result measured at a larger scattering angle of 40° for u-Be [10] indicates that the plasmon dispersion relation as predicted by the Mermin dielectric function has to be modified. The *ab initio* calculation of the plasmon dispersion relation and its measurement for WDM states via XRTS experiments will be the subject of future work.

Acknowledgments

We are grateful to the operators of the supercomputing center HLRN and the computing center of the University of Rostock for their assistance. This study was supported by the DFG within the SFB 652 and by the BMBF within the project 05K10HRA. This work was performed under the auspices of the US Department of Energy by Lawrence Livermore National Laboratory under contract no. DE-AC52-07NA27344 and supported by LDRD grant no. 10-ER-050. CF acknowledges support from the Alexander von Humboldt Foundation.

References

[1] Landen O L, Glenzer S H, Edwards M J, Lee R W, Collins G W, Cauble R C, Hsing W W and Hammel B A 2001 Dense matter characterization by x-ray Thomson scattering *J. Quant. Spectrosc. Radiat. Transfer* **71** 465

[2] Glenzer S H and Redmer R 2009 X-ray Thomson scattering in high energy density plasmas *Rev. Mod. Phys.* **81** 1625

[3] Baldis H A, Dunn J, Foord M E and Rozmus W 2002 Thomson scattering diagnostic of solid density plasmas using x-ray lasers *Rev. Sci. Instrum.* **73** 4223

[4] Glenzer S H *et al* 1999 Thomson scattering from high-Z laser-produced plasmas *Phys. Rev. Lett.* **82** 97

[5] Gregori G *et al* 2006 Measurement of carbon ionization balance in high-temperature plasma mixtures by temporally resolved x-ray scattering *J. Quant. Spectrosc. Radiat. Transfer* **99** 225

[6] Lee R W *et al* 2002 Plasma-based studies with intense x-ray and particle beam sources *Laser Part. Beams* **20** 527
[7] Lee R W *et al* 2003 Finite temperature dense matter studies on next-generation light sources *J. Opt. Soc. Am.* B **20** 770
[8] Glenzer S H, Gregori G, Lee R W, Rogers F J, Pollaine S W and Landen O L 2003 Demonstration of spectrally resolved x-ray scattering in dense plasmas *Phys. Rev. Lett.* **90** 175002
[9] Gregori G, Glenzer S H, Rozmus W, Lee R W and Landen O L 2003 Theoretical model of x-ray scattering as a dense matter probe *Phys. Rev.* E **67** 026412
[10] Glenzer S H *et al* 2007 Observations of plasmons in warm dense matter *Phys. Rev. Lett.* **98** 065002
[11] Glenzer S H *et al* 2008 Compton scattering measurements from dense plasmas *J. Phys.: Conf. Ser.* **112** 032071
[12] Lee H J *et al* 2009 X-ray Thomson-scattering measurements of density and temperature in shock-compressed beryllium *Phys. Rev. Lett.* **102** 115001
[13] Kritcher A L *et al* 2008 Ultrafast x-ray Thomson scattering of shock-compressed matter *Science* **322** 69
[14] Glenzer S H *et al* 2010 Dense plasma x-ray scattering: methods and applications *High Energy Density Phys.* **6** 1
[15] Kritcher A L, Döppner T, Fortmann C, Ma T, Landen O L, Wallace R and Glenzer S H 2011 In-flight measurements of capsule shell adiabats in laser-driven implosions *Phys. Rev. Lett.* **107** 015002
[16] Gregori G, Glenzer S H, Fournier K B, Campbell K M, Dewald E L, Jones O S, Hammer J H, Hansen S B, Wallace R J and Landen O L 2008 X-ray scattering measurements of radiative heating and cooling dynamics *Phys. Rev. Lett.* **101** 045003
[17] Fäustlin R R *et al* 2010 Observation of ultrafast non-equilibrium collective dynamics in warm dense hydrogen *Phys. Rev. Lett.* **104** 125002
[18] Höll A *et al* 2007 Thomson scattering from near-solid density plasmas using soft x-ray free electron lasers *High Energy Density Phys.* **3** 120
[19] Thiele R, Bornath Th, Fortmann C, Höll A, Redmer R, Reinholz H, Röpke G, Wierling A, Glenzer S H and Gregori G 2008 Plasmon resonance in warm dense matter *Phys. Rev.* E **78** 026411
[20] Glenzer S H, Gregori G, Rogers F J, Froula D H, Pollaine S W, Wallace R S and Landen O L 2003 X-ray scattering from solid density plasmas *Phys. Plasmas* **10** 2433
[21] Lindl J D, Amendt P, Berger R L, Glendinning S G, Glenzer S H, Haan S W, Kauffman R L, Landen O L and Suter L J 2004 The physics basis for ignition using indirect-drive targets on the national ignition facility *Phys. Plasmas* **11** 339
[22] Altmann M F, Mößbauer R L and Oberauer L J N 2001 Solar neutrinos *Rep. Prog. Phys.* **64** 97
[23] Höll A, Redmer R, Röpke G and Reinholz H 2004 X-ray Thomson scattering in warm dense matter *Eur. Phys. J.* D **29** 159
[24] Reinholz H, Redmer R, Röpke G and Wierling A 2000 Long-wavelength limit of the dynamical local-field factor and dynamical conductivity of a two-component plasma *Phys. Rev.* E **62** 5648
[25] Thiele R, Redmer R, Reinholz H and Röpke G 2006 Using the Gould–DeWitt scheme to approximate the dynamic collision frequency in a dense electron gas *J. Phys. A: Math. Gen.* **39** 4365
[26] Mermin N D 1965 Thermal properties of the inhomogeneous electron gas *Phys. Rev.* **137** 1441
[27] Röpke G, Redmer R, Wierling A and Reinholz H 1999 Response function including collisions for an interacting fermion gas *Phys. Rev.* E **60** R2484
[28] Selchow A, Röpke G, Wierling A, Reinholz H, Pschiwul T and Zwicknagel G 2001 Dynamic structure factor for a two-component model plasma. *Phys. Rev.* E **64** 056410
[29] Desjarlais M P 2003 Density-functional calculations of the liquid deuterium hugoniot, reshock and reverberation timing *Phys. Rev.* B **68** 064204
[30] Kietzmann A, Holst B, Redmer R, Desjarlais M P and Mattsson T R 2007 Quantum molecular dynamics simulations for the nonmetal-to-metal transition in fluid helium *Phys. Rev. Lett.* **98** 190602
[31] Holst B, Redmer R and Desjarlais M P 2008 Thermophysical properties of warm dense hydrogen using quantum molecular dynamics simulations *Phys. Rev.* B **77** 184201

[32] Desjarlais M P, Kress J D and Collins L A 2002 Electrical conductivity for warm, dense aluminum plasmas and liquids *Phys. Rev.* E **66** 025401
[33] Holst B, French M and Redmer R 2011 Electronic transport coefficients from *ab initio* simulations and application to dense liquid hydrogen *Phys. Rev.* B **83** 235120
[34] Chihara J 1987 Difference in x-ray scattering between metallic and non-metallic liquids due to conduction electrons *J. Phys. F: Met. Phys.* F **17** 295
[35] Chihara J 2000 Interaction of photons with plasmas and liquid metals—photoabsorption and scattering *J. Phys.: Condens. Matter* **12** 231
[36] Schwarz V *et al* 2010 Static ion structure factor for dense plasmas: semi-classical and *ab initio* calculations *High Energy Density Phys.* **6** 305
[37] Redmer R, Reinholz H, Röpke G, Thiele R and Höll A 2005 Theory of x-ray Thomson scattering in dense plasmas *IEEE Trans. Plasma Sci.* **33** 77
[38] Fortmann C, Wierling A and Röpke G 2010 Influence of local-field corrections on Thomson scattering in collision-dominated two-component plasmas *Phys. Rev.* E **81** 026405
[39] Ichimaru S and Utsumi K 1981 Analytic expression for the dielectric screening function of strongly coupled electron liquids at metallic and lower densities *Phys. Rev.* B **24** 7385
[40] Weinert M and Davenport J W 1992 Fractional occupations and density-functional energies and forces *Phys. Rev.* B **45** 13709
[41] Wentzcovitch R M, Martins J L and Allen P B 1992 Energy versus free-energy conservation in first-principles molecular dynamics *Phys. Rev.* B **45** 11372
[42] Kresse G and Hafner J 1993 *Ab initio* molecular dynamics for liquid metals *Phys. Rev.* B **47** 558
[43] Kresse G and Hafner J 1994 *Ab initio* molecular-dynamics simulation of the liquid–metal–amorphous–semiconductor transition in germanium *Phys. Rev.* B **49** 14251
[44] Kresse G and Furthmüller J 1996 Efficient iterative schemes for *ab initio* total-energy calculations using a plane-wave basis set *Phys. Rev.* B **54** 11169
[45] Blöchl P E 1994 Projector augmented-wave method. *Phys. Rev.* B **50** 17953
[46] Kresse G and Joubert D 1999 From ultrasoft pseudopotentials to the projector augmented-wave method *Phys. Rev.* B **59** 1758
[47] Perdew J P, Burke K and Ernzerhof M 1996 Generalized gradient approximation made simple *Phys. Rev. Lett.* **77** 3865
[48] Nosé S 1984 A unified formulation of the constant temperature molecular dynamics methods *J. Chem. Phys.* **81** 511
[49] Baldereschi A 1973 Mean-value point in the Brillouin zone *Phys. Rev.* B **7** 5212
[50] Kritcher A L *et al* 2009 Measurements of ionic structure in shock compressed lithium hydride from ultrafast x-ray Thomson scattering *Phys. Rev. Lett.* **103** 245004
[51] Wünsch K, Vorberger J and Gericke D O 2009 Ion structure in warm dense matter: benchmarking solutionsof hypernetted-chain equations by first-principles simulations *Phys. Rev.* E **79** 010201
[52] Gericke D O, Vorberger J, Wünsch K and Gregori G 2010 Screening of ionic cores in partially ionized plasmas within linear response *Phys. Rev.* E **81** 065401
[53] Kubo R 1957 Statistical-mechanical theory of irreversible processes. I. general theory and simpleapplications to magnetic and conduction problems *J. Phys. Soc. Japan* **12** 570
[54] Greenwood D A 1958 The Boltzmann equation in the theory of electrical conduction in metals *Proc. Phys. Soc.* **71** 585
[55] Monkhorst H J and Pack J D 1976 Special points for Brillouin-zone integrations *Phys. Rev.* B **13** 5188
[56] Recoules V and Mazevet S 2009 Temperature and density dependence of XANES spectra in warm dense aluminum plasma *Phys. Rev.* B **80** 064110
[57] Kremp D, Schlanges M and Kraeft W-D 2005 *Quantum Statistics of Nonideal Plasmas* (Berlin: Springer)